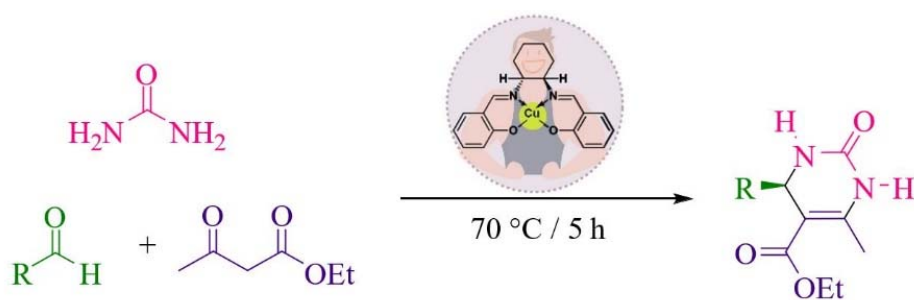


Chapter 4

DFT stimulation and experimental insights of chiral Cu(II)-salen scaffold within the pocket of MWW-zeolite and its catalytic study



4.1 Introduction

There have been numerous natural and synthetic bioactive substances developed using asymmetric synthetic techniques, including a multitude of total syntheses.¹ Multicomponent reactions (MCRs) can be used to synthesize organic compounds in a single step with a high atom economy. For instance, natural products have been synthesized using MCRs.² Despite the fact that chiral induction in MCRs is possible, it is not simple, and the selectivities that can be achieved aren't always ideal.³

As a method for preparing DHPMs, the multicomponent for instance, Biginelli-like reactions concerning aldehydes, urea and/or thiourea, and enolizable carbonyls have proven particularly effective. DHPMs can be used to treat infections and parasites like malaria,^{4,5} and they can also be used to reduce high blood pressure.⁶ Despite the Biginelli reaction's long history of discovery, asymmetric routes have received relatively little attention. It wasn't until 2003 when the reaction of urea, benzaldehyde, and methyl acetoacetate with cerium(III) chloride utilizing a chiral amide was first described; this reaction was facilitated by Juaristi and Muoz-Muiz.⁷ Despite this, the enantiomeric excess (ee) that was achieved was just 40%. The asymmetric Biginelli reaction, which uses a chiral ytterbium catalyst to achieve high enantioselectivities (>99% ee), was next described by Zhu.⁸ Gong later described the foremost organocatalytic Biginelli reaction, which provided DHPMs with ee values as high as 97% by employing chiral phosphoric acids obtained from 1,1'-bi-2-naphthol (BINOL) as catalysts.⁹ However, there are drawbacks, such as the need for extremely hazardous organic solvents, a significant amount of catalyst, severe reaction conditions, and a lot of time and effort spent on separating the target product.

Therefore, there is a need for the creation of straightforward Biginelli techniques that are gentle and environment caring, and recently, some intriguing environmentally friendly processes have been developed. As formerly reported, there are numerous reliable and intriguing techniques for the enantioselective, Bronsted acid-catalyzed synthesis of DHPMs. These reactions, however, are typically carried out in organic solvents; catalysts are not retrieved and used again, as well as target DHPMs are purified using column chromatography. As a result, there needs to be more

focus on creating an eco-friendly and enantioselective Biginelli protocol using a Bronsted acid catalyst.

Bhaumik and colleagues have created an ordered mesoporous material functionalized with phosphonic acid groups. This material is applicable in solvent-free conditions for conducting one-pot multicomponent Biginelli reactions, yielding 92%.¹⁰ Maleki A. and his colleagues¹¹ have reported a new-fangled magnetic Fe₃O₄-halloysite-SO₃H nanocomposite with nanotube morphology. The as-synthesized porous catalyst was efficaciously used to prepare dihydropyrimidinones with 96% yield using an aldehyde, β -ketoester and urea or thiourea as starting substrates. Hence, there is increased interest in the development of an environmentally friendly and enantioselective Biginelli protocol catalyzed by a Bronsted acid.¹²

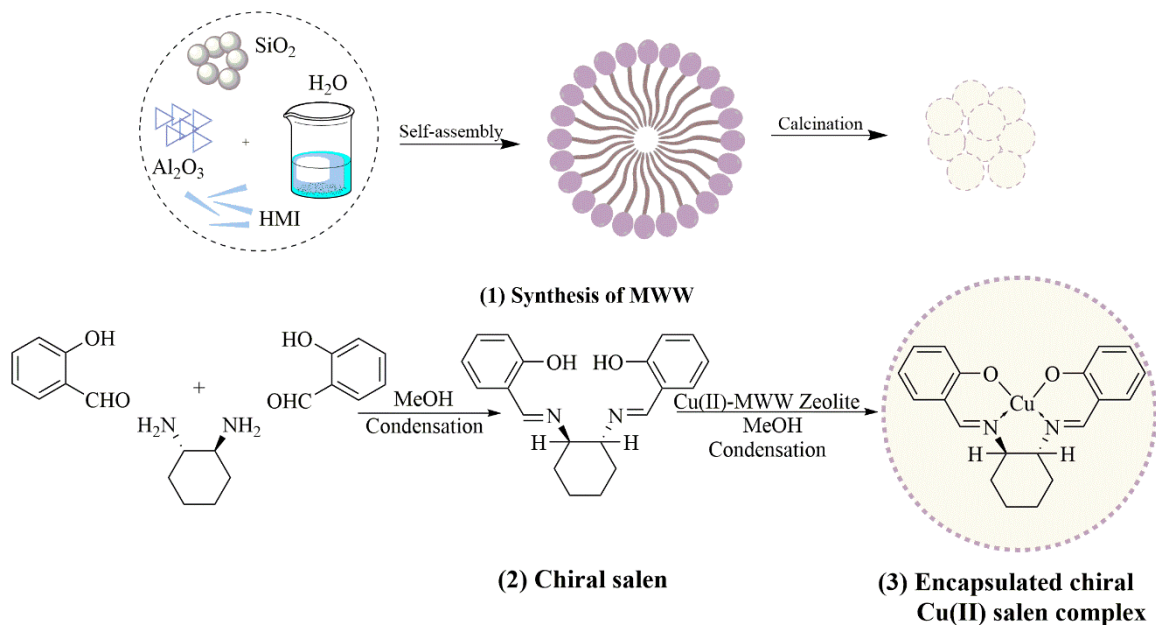
The use of porous solids in catalysis and sorption has led to a number of breakthroughs and innovations.¹³ A number of key new areas, including green chemistry and environmental catalysis, are currently driven by processes that use porous catalysts.¹⁴ Materials with pore structures containing micro- or meso-pores with molecular dimensions have proved to be most effective in terms of activity and performance.¹⁵ Considering their exceptional catalytic properties, transition metal schiff base complexes have been identified as propitious contenders for C-C bond formation. These homogeneous schiff base complexes are typically immobilized on alumina, silica, or zeolites in order to improve catalyst stability, facilitate the recycling of catalysts and product separation easier.^{16,17}

On microporous materials like zeolites, Schiff base complexes can be heterogenized, but this limits the size of the complexes and significantly leaches the catalysts. On the other hand, mesoporous silica substances have been widely utilized as valuable and adaptable solid bases for producing an extensive variety of hybrid substances in catalysis, immobilizing enzymes, and delivering drugs. This is due to their significant and modifiable pore sizes, substantial surface areas, and various possibilities for surface functional modification. Hence, observing the covalent bonding of Schiff base complexes onto a functionally modified siliceous mesoporous material with remarkably spacious pores is intriguing.¹⁸⁻²⁴

Strategies based on mesopores silica appear more appealing due to their eco-friendliness.²⁵ However, some of these methods necessitate the use of costly reagents, higher acidic conditions, extended reaction periods, high temperatures, stoichiometric concentrations of catalysts, or the generation of unwanted byproducts like pollution or subpar yields. Efforts to increase productivity and decrease reaction times were also detailed and fine-tuned. However, this response is not without its significant downsides. Constraints of the enantioselective Biginelli MCRs include low yields, long reaction durations (usually 7 days), low ee's, the catalysts' production requiring many synthetic stages, and others.^{26–28}

The current development in the field of porous MWW-based catalysts is mainly focused on improving diffusion and catalytic activity as well as capturing bulkier molecules inside the pores.^{29–31} Choudhary A. and coworkers have developed encapsulated Ni salen complexes in zeolite Y, and comparative characterizations have been conducted using DFT and experimental results.³² The chiral Ni-Schiff base complex confined within zeolite-Y has been and assessed in the context of the asymmetric reaction. This reported by Sharma M and his colleagues.³³ The energy barrier of this encapsulated metal complex has been carried out using density functional theory (DFT). Co(II) Schiff base complexes in zeolite-Y were investigated by Kumari S. and her colleagues using DFT and experimental methods.³⁴ In summary, these complexes have demonstrated high reusability and stability in zeolite-Y, making them attractive for industrial applications.

In light of the previous efforts undertaken,^{35–38} herein this chapter, report for the first time the encapsulation of chiral Cu(II)-salen complexes inside MWW-framework zeolite pores and tested for one-pot multicomponent Biginelli reaction in liquid phase (*Scheme 4.1*). In order to grasp the inherent alterations in the structure and electronic properties of complexes induced by the MWW zeolite framework, a density functional theory (DFT) has been employed. Based on theoretical and experimental evidences, chiral Cu(II)-salen complex and MWW zeolite interact well after encapsulation.



Scheme 4.1 A schematic representation for the synthesis of MWW (1), Chiral salen (2) and Encapsulated chiral Cu(II) salen complex (3).

4.2 Experimental

4.2.1 Preparation of MWW zeolite:

MWW zeolite was synthesized using a previously described procedure³⁹⁻⁴¹, in which a gel mixture with the molar ratios $\text{SiO}_2/\text{Al}_2\text{O}_3 = 30$, $\text{Na}/\text{SiO}_2 = 0.18$, $\text{HMI}/\text{SiO}_2 = 0.35$ (where HMI = hexamethyleneimine as a template), and $\text{H}_2\text{O}/\text{SiO}_2 = 20.5$ was heated at 150 °C for 7 days with rotation (30 rpm). The layered MWW precursor was filtered out and dried at 100 °C before being calcined at 550 °C for 6 hours to produce MWW zeolite. (Scheme 4.1).

4.2.2 Synthesis of chiral salen Schiff base ligand:

A chiral salen ligand was prepared by dropwise addition of (-)-trans-1,2-diaminocyclohexane (2.5 mmol) to a 10 mL methanolic solution of salicylaldehyde (5 mmol). Following 30 minutes of stirring in an ice-water bath fitted with a condenser, 3 hours of heating at

reflux temperature, and finally cooling to room temperature, a yellow precipitate of the product was obtained. The product was dissolved in dichloromethane, then washed with 10×2 distilled water, then 7×2 brine solution, the organic layer was allowed to dry overnight on bed of sodium sulphate, the solvent is removed, and the product is collected.⁴²⁻⁴⁴

4.2.3 Synthesis of metal exchange MWW zeolite:

A continuous stir was maintained at 90 °C for 24 h while 5 g of MWW zeolite was dispersed in 300 ml of distilled water comprising of 12 mmol Cu(II) salt. The end result underwent filtration, followed by a comprehensive hot distilled water rinse to remove any remaining metal ions. Afterward, it was dried at 120 °C for a duration of 15 hours.^{45,46}

4.2.4 Preparation of chiral Cu(II)-salen complex encapsulated in MWW zeolite:

Cu(II) exchanged MWW zeolite was thoroughly mixed with an abundance of chiral salen ligand (metal/ligand=0.33) and sealed in a round bottom flask. There was only adequate solvent present to cover the mixture. The mixture was then refluxed for 24 hours with nitrogen gas flow through it. Non-reacted ligands were extracted with acetone, and free Cu(II) ions were eliminated through ion-exchange with 0.1 M NaCl solution. The sample was then thoroughly washed with distilled water, and dried in an air oven for 60 min to obtain the chiral Cu(II)-salen complex encapsulated in MWW zeolite⁴⁷⁻⁵² (*Scheme 4.1*)

4.2.5 Determination of the chiral salen ligand crystal structure

To acquire three-dimensional X-ray intensity data, a crystal with suitable morphology was selected. Data collection was performed at 100K using a Rigaku Oxford Diffraction X-ray diffractometer equipped with CuK α radiation ($\lambda=1.54184$ Å). Cell dimensions were determined through a least-squares fitting approach involving 6011 reflections spanning angular settings in the range of θ from 4.707° to 72.319°. A total of 13105 reflections were recorded for θ ranging from 4.720° to 67.045°, with 2932 of them being unique. Out of these, 2865 reflections were considered as observed ($I > 2\sigma(I)$). Subsequent adjustments were made to the data for Lorentz-

polarization and absorption corrections. The achieved values of $R_{\text{int}} = 0.0389$ and $R_{\text{sigma}} = 0.0302$ affirm the acceptable quality of the collected data.

The title compound exhibits crystallization within the monoclinic system, featuring the Cc space group. The crystal structure of the chiral salen ligand was determined using direct methods. The positions of the non-hydrogen atoms within the molecule were determined using the highest-quality E-map, and their arrangement was refined using an anisotropic approximation via SHELXS.⁵³ An oxygen H atoms' positioning was established using a difference Fourier map. For hydrogen atoms attached to carbon atoms, their positions were constrained and allowed to ride on the respective non-H atoms, adhering to geometric criteria [$\text{C-H} = 0.93\text{-}0.98 \text{ \AA}$, and $U_{\text{iso}}(\text{H}) = 1.2$ times U_{eq} of the corresponding C atoms]. Four cycles of full-matrix least-squares refinement were iterated, ultimately yielding final R-factor and GOOF values of 0.0311 and 1.037, respectively.

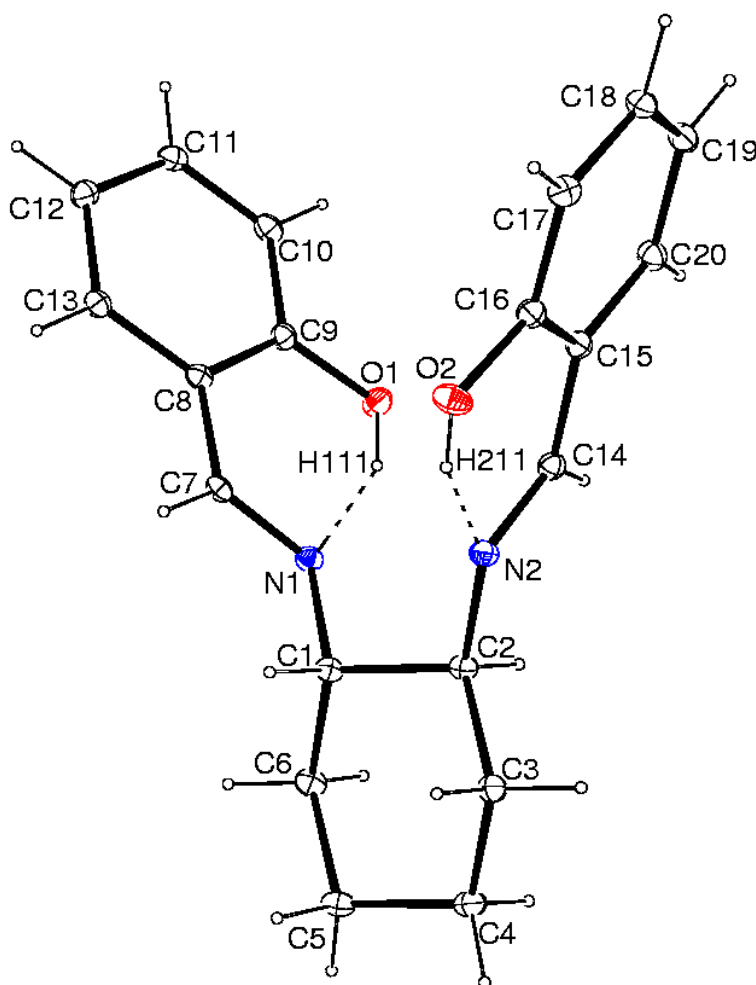
The remaining electron density evident in the ultimate difference Fourier map was within the range of $-0.150 < \Delta\rho < 0.141$. *Figure 4.1* illustrates an ORTEP representation of the compound, complete with atomic labeling.⁵⁴ WinGX,⁵⁵ and PLATON⁵⁶ software were employed to compute the molecular geometry of the title compound. The pertinent crystallographic information, along with details of structure determination and refinement for the title compound, are presented in *Table 4.1*. *Table 4.2* provides an overview of the hydrogen bonding network. Additionally, *Figure 4.2* offers a visual representation of the molecular arrangement within the unit cell along the b-axis.

Table 4.1 Crystal and experimental data

CCDC No	2181683
Crystal description	Yellow, Prism
Empirical formula	C ₂₀ H ₂₂ N ₂ O ₂
Formula weight	322.39
Radiation, wavelength	CuK α , 1.54184 Å
Unit cell dimensions	a = 15.7967(3), b = 11.6889(2), c = 9.4813(2) Å, β = 97.276(2)°
Crystal system	Monoclinic
Space group	<i>Cc</i>
Unit cell volume	1736.59(6) Å ³
Density (calculated)	1.233 Mgm ⁻³
No. of molecules per unit cell, <i>Z</i>	4
Temperature	100(2) K
Absorption coefficient	0.637 mm ⁻¹
<i>F</i> (000)	688
Scan mode	ω scan
θ range for entire data collection	4.720° to 67.045°
Range of indices	-18 $\leq h \leq$ 18, -13 $\leq k \leq$ 13, -10 $\leq l \leq$ 11
Reflections collected /unique	13105/2932
Reflections observed (<i>I</i> > 2 σ (<i>I</i>))	2865
R _{int}	0.0389
R _{sigma}	0.0302
Structure determination	Direct methods
Refinement	Full-matrix least-squares on <i>F</i> ²
No. of parameters refined	223
Final <i>R</i>	0.0311
w <i>R</i> (<i>F</i> ²)	0.0767
Weight	1/ [$\sigma^2(F_o^2) + (0.0421P)^2 + 0.4185P$] where $P = [F_o^2 + 2F_c^2] / 3$
Goodness-of-fit	1.037
(Δ/σ) _{max}	0.000
Final residual electron density	-0.150 < $\Delta\rho$ < 0.141 e Å ⁻³
Computing_cell_refinement	'CrysAlisPro 1.171.42.36a (Rigaku OD, 2021)'
Computing_data_collection	'CrysAlisPro 1.171.42.36a (Rigaku OD, 2021)'
Computing_data_reduction	'CrysAlisPro 1.171.42.36a (Rigaku OD, 2021)'
Computing_structure_solution	'SHELXT 2018/2 (Sheldrick, 2015)'
Computing_structure_refinement	'SHELXL-2018/3 (Sheldrick, 2015)'
Computing_molecular_graphics	'ORTEP3 (Farrugia, 2012)'
Computing_publication_material	'PLATON (Spek,2009)'

Table 4.2 O-H...N intramolecular hydrogen bonding geometry.

D-H...A	D-H(Å)	H...A(Å)	D...A(Å)	q [D-H...A(°)]
O1-H111...N1	0.84	1.85(2)	2.605(3)	148(3)
O2-H211...N2	0.83	1.85(2)	2.608(3)	151(3)

**Figure 4.1** ORTEP view of the molecule with displacement ellipsoids drawn at 50% probability level.

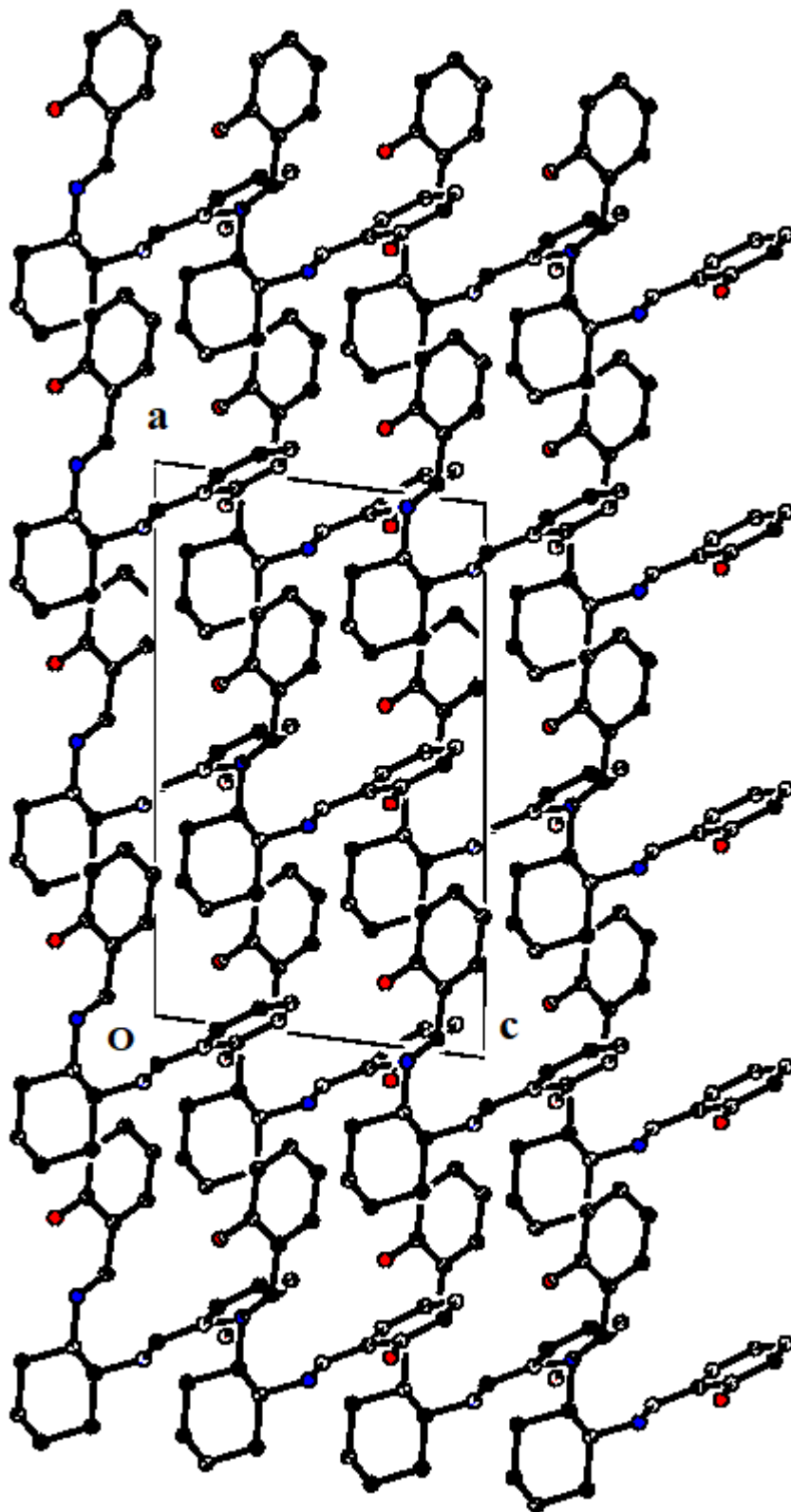


Figure 4.2 Packing arrangement of molecules viewed down the b-axis.

4.2.6 Catalytic activity:

Using a chiral Cu(II) salen complex encapsulated within MWW zeolite, a proficient catalytic process for the asymmetric Biginelli derivatives was developed. In a round bottom flask (RBF), aldehyde, ethyl acetoacetate, and urea were combined and reacted with an encapsulated chiral Cu(II) salen catalyst under an argon atmosphere at 70 °C. After the reaction was finished, the heterogeneous catalyst was isolated through filtration. The resulting filtrate was then mixed with crushed ice once it had cooled to room temperature, yielding a solid residue comprising the desired 3,4-dihydropyrimidinones. The separated catalyst was suspended in ethyl alcohol and stirred at room temperature for 30 minutes. Subsequently, it was filtered and subjected to drying in an oven at 60 °C for 1.5 hours, rendering it ready for reuse in subsequent runs.^{57–63}

4.3 Results and Discussion

4.3.1 X-ray Diffraction Patterns

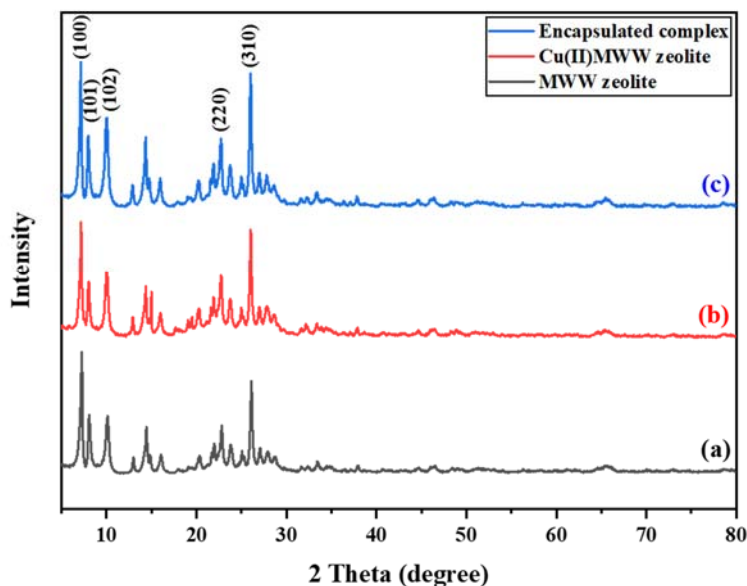


Figure 4.3 XRD patterns (a) MWW zeolite (b) Cu(II)-MWW zeolite and (c) encapsulated chiral Cu(II) salen catalyst

The crystallinity of the as-prepared samples must be ascertained using the X-ray powder diffraction (XRD) technique. *Figure 4.3* (a), (b), and (c) show XRD patterns of the MWW zeolite, Cu(II)-MWW zeolite, and the encapsulated chiral Cu(II) salen catalyst, respectively. The ordered structure is preserved throughout the grafting process, as evidenced by the presence of distinctive MWW zeolite diffraction peaks at 2θ of 7.2° , 8.0° , 9.6° , 25° , and 26° , assigned to (100), (101), (102), (220), and (310) reflections, respectively, in all the samples.^{64,65}

4.3.2 Scanning electron microscopy

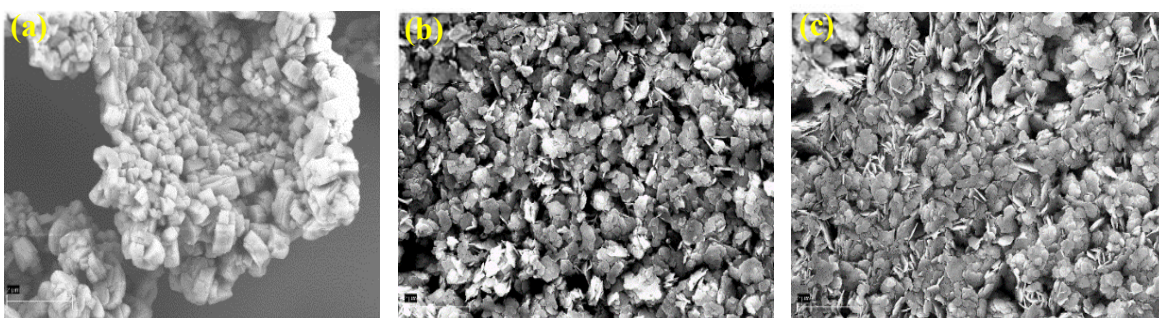


Figure 4.4 FESEM images of (a) MWW zeolite (b) Cu(II)-MWW zeolite and (c) encapsulated chiral Cu(II) salen catalyst.

Figure 4.4 shows FESEM images of MWW zeolite, Cu(II)-MWW zeolite, and encapsulated chiral Cu(II) salen catalyst. MWW zeolite primary crystals exhibit the well-known platelet morphology [*Figure 4.4(a)*]. Similar particle size, as seen in *Figure 4.4(b)* and (c), demonstrating that the addition of copper and salen ligand caused only minor changes in the textural properties of MWW zeolite crystals.^{66–68}

4.3.3 BET analysis

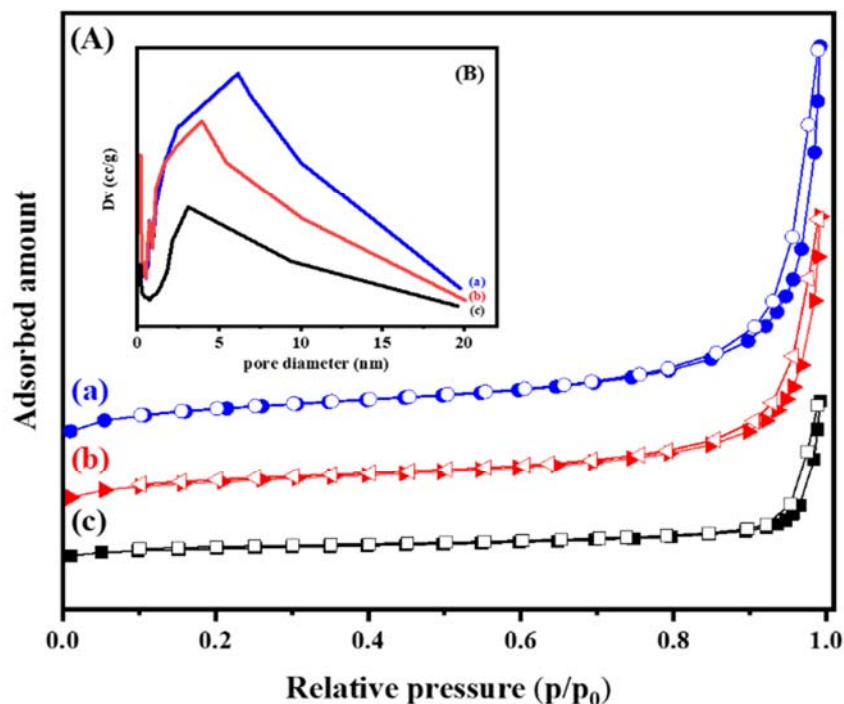


Figure 4.5 (A) N_2 adsorption–desorption isotherms of (a) MWW zeolite (b) Cu(II)-MWW zeolite and (c) encapsulated chiral Cu(II) salen catalyst; (B) BJH pore size distributions of (a) MWW zeolite (b) Cu(II)-MWW zeolite and (c) encapsulated chiral Cu(II) salen catalyst.

Table 4.3 Textural parameters of catalyst

Sample	Surface area/ $m^2 g^{-1}$	Pore volume/ $cm^3 g^{-1}$	Average pore diameter/nm
MWW zeolite	415.45	0.52	6.1
Cu(II)-MWW zeolite	291.36	0.50	3.9
Encapsulated chiral Cu(II)-salen catalyst	28.52	0.16	3.4

The N₂ adsorption/desorption isotherms and the BJH pore size distributions of MWW zeolite, Cu(II)-MWW zeolite, and encapsulated chiral Cu(II) salen catalyst samples are shown in *Figure 4.5* (A) and (B), respectively. The ordered mesoporous structure of the MWW zeolite is preserved in the hybrid materials, which also retain the type IV isotherm properties and have a uniform pore size distribution. However, the pore diameter of pure MWW zeolite decreases from 6.1 nm to about 3.9 nm for Cu(II)-MWW zeolite and 3.4 nm for encapsulated chiral Cu(II) salen catalyst. As shown in *Table 4.3*. The BET surface area gradually decreases, indicating that these organic scaffolds were successfully encapsulated into the MWW zeolite framework.^{69,70}

4.3.4 FTIR spectra

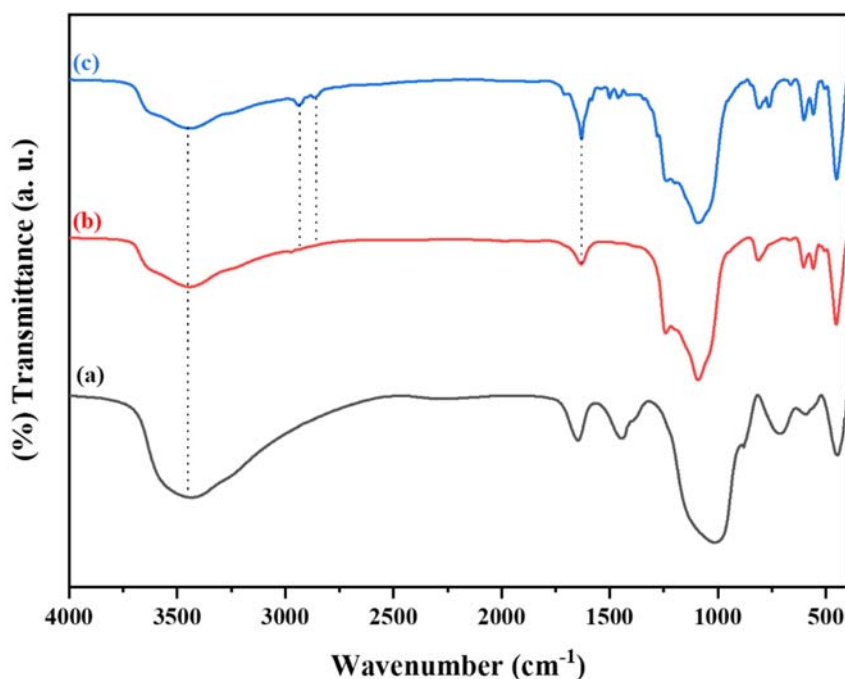


Figure 4.6 FTIR spectra of (a) MWW zeolite; (b) Cu(II) MWW zeolite; (c) encapsulated chiral Cu(II)-salen catalyst.

The FTIR spectra of MWW zeolite, Cu(II)-exchanged MWW zeolite, and encapsulated chiral Cu(II)-salen catalyst are shown in *Figure 4.6*. The FTIR spectrum of MWW zeolite displays

a strong broad band at 1000 cm^{-1} owing to the asymmetric stretching vibration of $(\text{Si}/\text{Al})\text{O}_4$ units. Due to low concentrations of the chiral $\text{Cu}(\text{II})$ -salen complex inside the cavities of MWW zeolite, the intensities of IR bands of encapsulated complex is weak. In the FTIR spectrum of an encapsulated complex, there is a broad band in the range of $3430\text{--}3449\text{ cm}^{-1}$, accompanied by two fainter bands in the ranges of $815\text{--}840\text{ cm}^{-1}$ and $670\text{--}690\text{ cm}^{-1}$, which are thought to be $-\text{OH}$ stretching, rocking, and wagging vibrations, respectively. This suggests that hydrated water molecules.⁷¹

4.3.5 UV-vis spectra

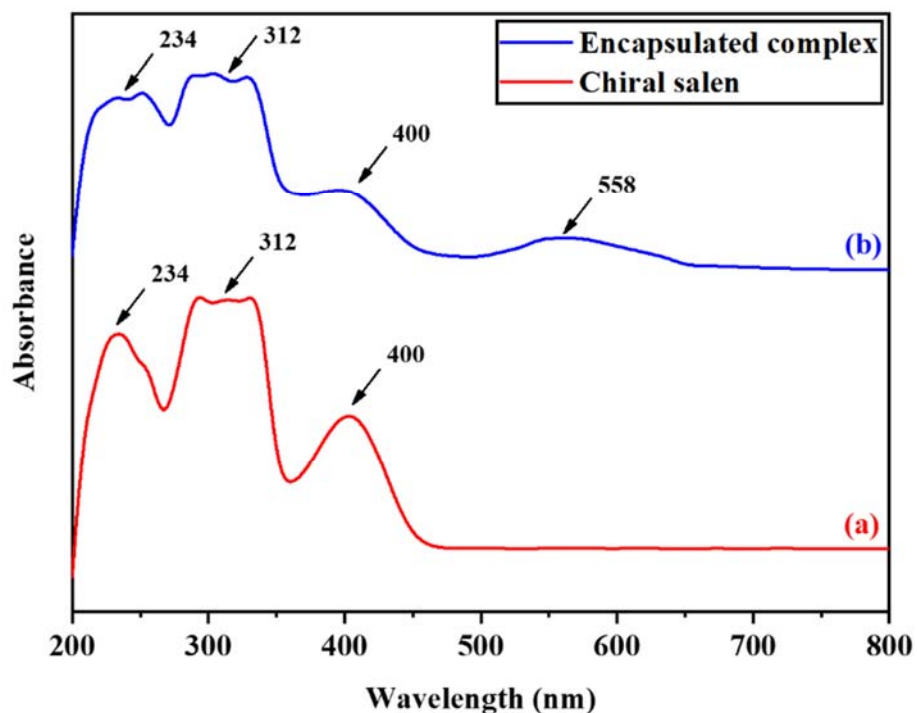


Figure 4.7 UV-vis spectra of (a) chiral salen (b) encapsulated chiral $\text{Cu}(\text{II})$ salen

Figure 4.7 depicts the UV-vis spectra of chiral salen and encapsulated chiral $\text{Cu}(\text{II})$ salen catalyst. The bands at 234 and 400 nm are attributed to $\pi\text{--}\pi^*$ located predominantly on the phenyl ring, and the peak at 312 nm is attributed to C-N. The expected $d\text{--}d$ transition of encapsulated

chiral Cu(II) salen at 568 nm was also observed, confirming its formation within the MWW zeolite materials.²³

4.3.6 EDAX spectra

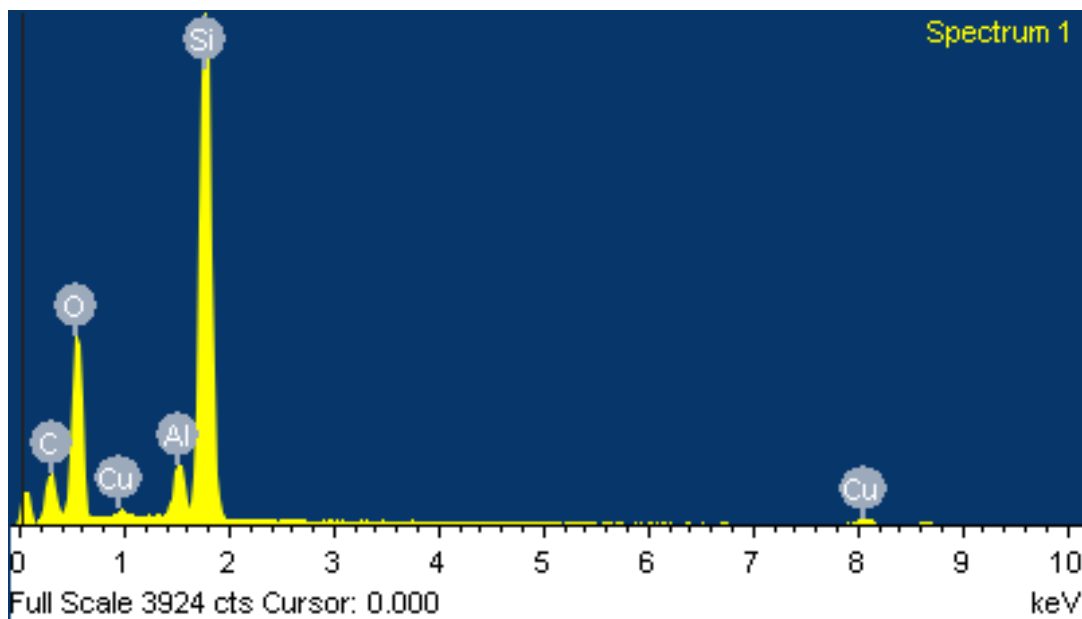


Figure 4.8 EDAX spectra of encapsulated chiral Cu(II)-salen catalyst

The EDAX analysis confirms the presence of all elements (Cu, Si, Al, and O) in the structure of encapsulated chiral Cu(II)-salen catalyst (*Figure 4.8*).^{72,73}

4.3.7 X-ray photoelectron spectroscopy

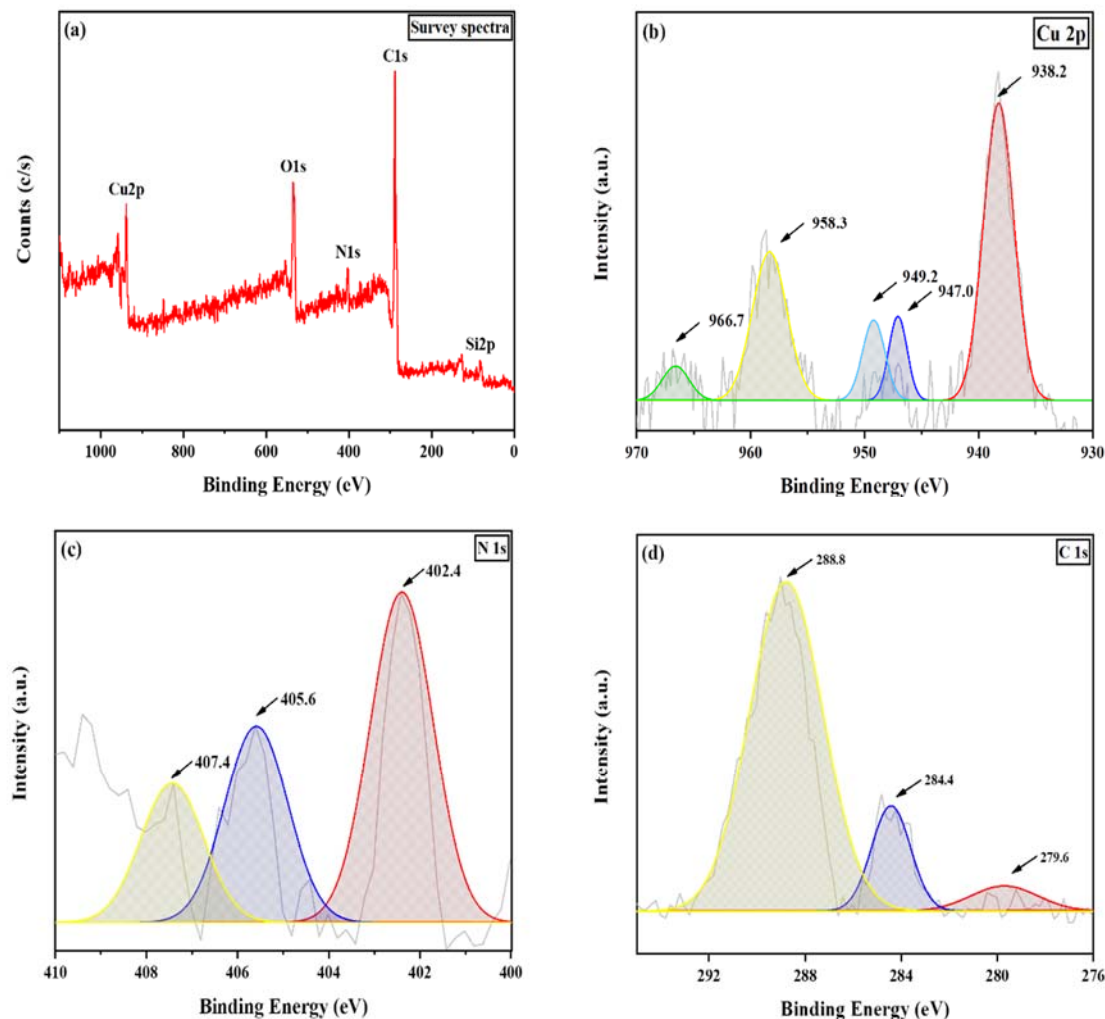


Figure 4.9 XPS analysis of the encapsulated chiral Cu(II) salen; (a) survey spectra, (b) Cu 2p, (c) N 1s and (d) C 1s.

XPS was employed to examine the elemental composition and bonding configuration on the surface of the synthesized chiral Cu(II)-salen catalyst encapsulated within the structure. The full scan XPS spectrum, presented in *Figure 4.9(a)*, clearly reveals the presence of Cu, O, N, C, and Si elements. Specific to the Cu 2p region, as depicted in *Figure 4.9(b)*, characteristic peaks situated at 938.2 and 958.3 eV are identified, corresponding to Cu(II) states—specifically Cu 2p_{3/2} and Cu 2p_{1/2}, respectively. When a valence electron interacts with an outgoing electron, the core

electron's energy is reduced, and a satellite structure appears in Cu 2p_{3/2} and Cu 2p_{1/2} regions at around 947 eV and 966.7 eV (*Figure 4.9(b)*) as a result of the open 3d⁹ valence shells of Cu²⁺ species, indicating copper's bivalent oxidation state.^{74,75} Furthermore, the introduction of copper oxide could potentially account for the perturbation observed in the satellite peak near 949.2 eV within the Cu 2p XPS spectrum. This observation suggests a heightened reactivity of copper on the catalyst's surface and its capability to transition between diverse oxidation states. These dynamics play a role in enhancing the catalytic efficiency of the system. The interaction between the copper and nitrogen moieties of carbon resulted in three peaks in the N 1s spectrum (*Figure 4.9(c)*) at 402.4 eV (CN), 405.6 eV, and 407.4 eV. In the C 1s spectrum (depicted in *Figure 4.9(d)*), a trio of well-defined peaks emerges at 279.6, 284.4, and 288.8 eV. These peaks correspondingly correspond to distinct chemical bonds: CH_x or C-C, C-O or C-N, and C=N.⁷⁶⁻⁷⁸

4.4 Theoretical studies & results

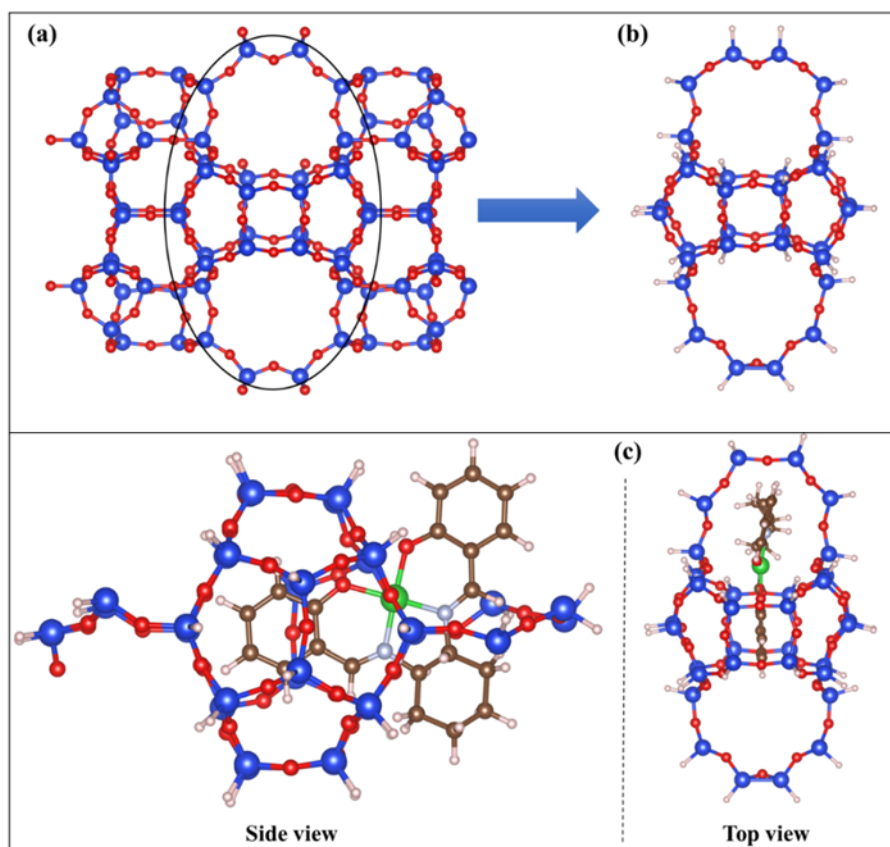


Figure 4.10 The MWW zeolite (a) and (b) and MWW zeolite encapsulated Cu(II)-salen complex (c), respectively.

All calculations of Cu(II)-salen complex, MWW zeolite and MWW zeolite encapsulated Cu(II)-salen complex were performed under the set-up of density functional theory (DFT) by Quantum Espresso package.⁷⁹ To incorporate the electron exchange-correlation potential, the generalized gradient approximation from Perdew-Burke-Ernzerhof (PBE) was utilized.⁸⁰ For all calculations, kinetic energy cut-off of 680 eV was chosen. It was decided to use a convergence criteria of 10^{-4} eV for total energy and to perform self-consistent convergence until the maximum Hellmann-Feynman forces acting on each atom became less than 0.001 eV/Å. Visualization of the structural geometry are performed using VESTA software.⁸¹

Figure 4.10(a) illustrates the geometry of the MWW zeolite.⁸² Firstly, we have performed relaxation calculation for cleaved MWW zeolite (see *Figure 4.10(b)*) and which was considered for further study. The dangling bonds of the cleaved geometry is saturated with the H atoms. Furthermore, we have also performed relaxation calculation for Cu(II)-salen complex independently. After fully relaxation of the MWW zeolite and Cu(II)-salen complex, we have inserted the Cu(II)-salen complex into the MWW zeolite and again performed the relaxation calculation. Two different views of the MWW zeolite encapsulated Cu(II)-salen complex are represented in *Figure 4.10(c)*. Structural geometry of the *Figure 4.10(c)* suggests that the encapsulation of the Cu(II)-salen complex in MWW zeolite is possible with retaining chirality of the Cu(II)-salen complex after the interaction.

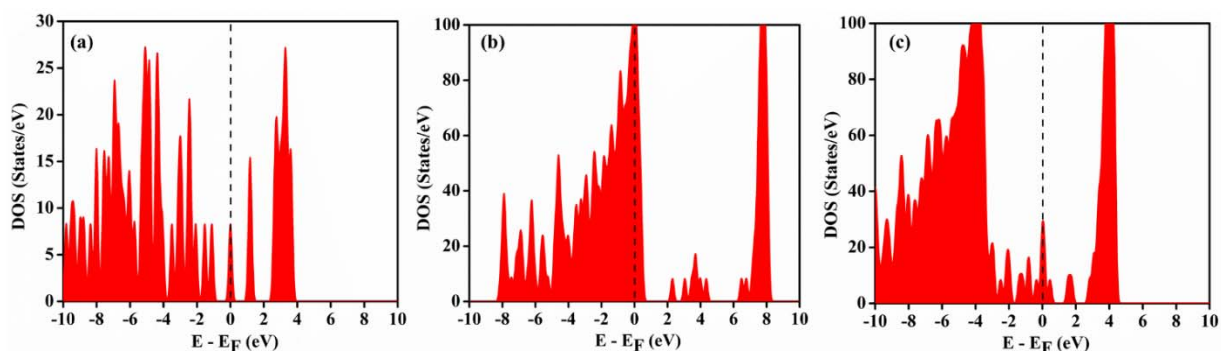


Figure 4.11 The density of states plot of the Cu(II)-salen complex (a), MWW zeolite (b) and MWW zeolite encapsulated Cu(II)-salen complex (c), respectively.

The binding energy (E_{bin}) has been calculated to confirm the encapsulation of the Cu(II)-salen complex within the MWW zeolite. The E_{bin} is calculated from the following formula:

$$E_{bin} = E(\text{Cu(II)-salen complex} + \text{MWW}) - E(\text{Cu(II)-salen complex}) - E(\text{MWW}) \text{ -----(1)}$$

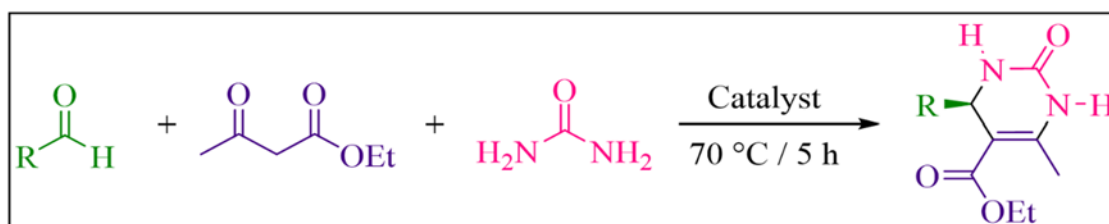
where $E(\text{Cu(II)-salen complex} + \text{MWW})$, $E(\text{Cu(II)-salen complex})$ and $E(\text{MWW})$ are the total energy of MWW zeolite encapsulated Cu(II)-salen complex, Cu(II)-salen complex and MWW zeolite, respectively.⁸³ In general, the negative value of calculated E_{bin} indicates the significant interaction of Cu(II)-salen complex with MWW zeolite and positive value of E_{bin} indicates very poor interaction (not possible) of Cu(II)-salen complex with MWW zeolite.

In present study, the calculated E_{bin} (using equation 1) is -4.75 eV which ensures good interaction between Cu(II)-salen complex and MWW zeolite. Furthermore, structural changes are very obvious after strong interaction between Cu(II)-salen complex and MWW zeolite. After relaxation of Cu(II)-salen complex into the MWW zeolite, bond lengths Cu-O and Cu-N of Cu(II)-salen complex became 1.93 Å and 1.92 Å from 1.91 Å and 1.97 Å, respectively. Bond length of Si-O is also changed near adsorbed area. In addition, when we compared the structural geometries of the MWW zeolite (See *Figure 4.10(b)*) and MWW zeolite encapsulated Cu(II)-salen complex (See *Figure 4.10(c)*), others minor structural changes are also visible from the naked eyes.

To validate the interaction, we have also calculated and analyzed the density of states (DOS) plots for the Cu(II)-salen complex (see *Figure 4.11(a)*), MWW zeolite (see *Figure 4.11(b)*) and MWW zeolite encapsulated Cu(II)-salen complex (see *Figure 4.11(c)*), respectively. *Figure 4.11* clearly depicts the enhancement in intensity of states in the bonding region of MWW zeolite after encapsulation of the Cu(II)-salen complex (*Figure 4.11(c)*) compared to neat the MWW zeolite (*Figure 4.11(b)*). These enhancement of states in the bonding region indicates good interaction between Cu(II)-salen complex and MWW zeolite after encapsulation and also validates the calculated E_{bin} .

4.5 Catalytic activity

The multicomponent Biginelli reaction was used in the catalytic test for the synthesis of DHPMs (*Scheme 4.2*). The amount of product obtained after recrystallization was used to calculate the reaction yield. Hence, the yield is determined by dividing the mass of the obtained product by the theoretical maximum amount and expressing it as a ratio. Thin layer chromatography (TLC) revealed that the catalyst accomplished a 94% conversion with 91.92% ee selectivity (Turnover number (TON): 20,042) of the multicomponent reaction after 5 hours, which was adequate time to discontinue the reaction (*Table 4.4*). In order to improve the DHPMs synthesis methodology, the influences of temperature, reaction time, and the quantity of catalyst were examined. Encapsulated chiral Cu(II) salen complex, the catalyst with the optimal recital under the experimental conditions of the model reaction, was used for this purpose. Then, various substrates were evaluated using this methodology. The results are shown in *Table 4.4*.



Scheme 4.2 Asymmetric Biginelli Reaction catalyzed by encapsulated chiral Cu(II) salen catalyst.

4.5.1 Benzaldehyde derivatives

As shown in *Table 4.4*, the product yields varied between 91.7% and 96.1% across all reactions, encompassing diverse aromatic aldehydes featuring donor or electron acceptor substituents. From above results, it appears that the substituents affect the reactivity of the carbonyl group within the aromatic aldehyde, potentially impacting the quantity of product generated. The yields of aromatic aldehydes bearing electron-donating groups were comparatively lower than those of benzaldehyde and aldehydes carrying electron-withdrawing substituents. It's worth noting that even though 4-nitrobenzaldehyde (*Table 4.4*, entry 3) possesses a potent electron-withdrawing group, it resulted in a higher yield compared to aldehydes substituted with electron-donating

groups. It is through the nitro group that the carbonyl group acquires an electrophilic character, thereby increase in reactivity can be attributed to its heightened susceptibility to nucleophilic chemical species.

Table 4.4 DHPMs synthesized via multicomponent Biginelli reaction using various substrates

Entry	Substrates(R)	Conversion(%)	ee (%) ^a	M. P. (°C)	TON ^b
1	C ₆ H ₅	94.0	91.92	210-211	20,042
2	4-CH ₃ -C ₆ H ₄	93.7	86.64	204-205	19,978
3	4-NO ₂ -C ₆ H ₄	96.1	82.94	210-211	20,490
4	4-OH-C ₆ H ₄	91.7	85.97	232-234	19,552

^a ee Determined by chiral-phase HPLC analysis (Chiralpak OJ-H); Reaction condition: aldehydes (1.0 mmol), ethyl-acetoacetate (1.0 mmol), urea (1.2 mmol), HAc (10 mL), and encapsulated chiral Cu(II) salen (0.15 g), 70 °C, 5 h.

^b TON (turnover number) = Moles of desired product formed/number of active centers.

4.5.2 Recyclability test

To investigate the possibility of reusing the encapsulated chiral Cu(II)-salen catalyst in chiral DHPM synthesis, the stability of the catalyst was evaluated. The catalyst was reclaimed from the reaction through the process of filtration, then suspended in EtOH (2 mL) and agitated for 30 minutes at room temperature. To prepare it for future experiments, it was filtered and dried in an oven at 60 °C for 1.5 hours. The recyclability test of an encapsulated chiral Cu(II)-salen catalyst over chiral DHPM synthesis is shown in *Figure 4.12*, and the results are tabulated in *Table 4.5*. This catalyst was found to be stable and could be reused for five times before significant reductions in product yield, confirming that it could be utilized for multicomponent Biginelli reaction.

Table 4.5 Recyclability data of the DHPM synthesis.

Entry	Conversion (%)	ee (%) ^a	TON ^b
1	94.0	91.92	20,042
2	93.7	90.80	19,978
3	92.1	86.25	19,637
4	89.8	85.36	19,147
5	86.2	83.53	18,379

^a ee Determined by chiral-phase HPLC analysis (Chiralpak OJ-H); ^b TON (turnover number)

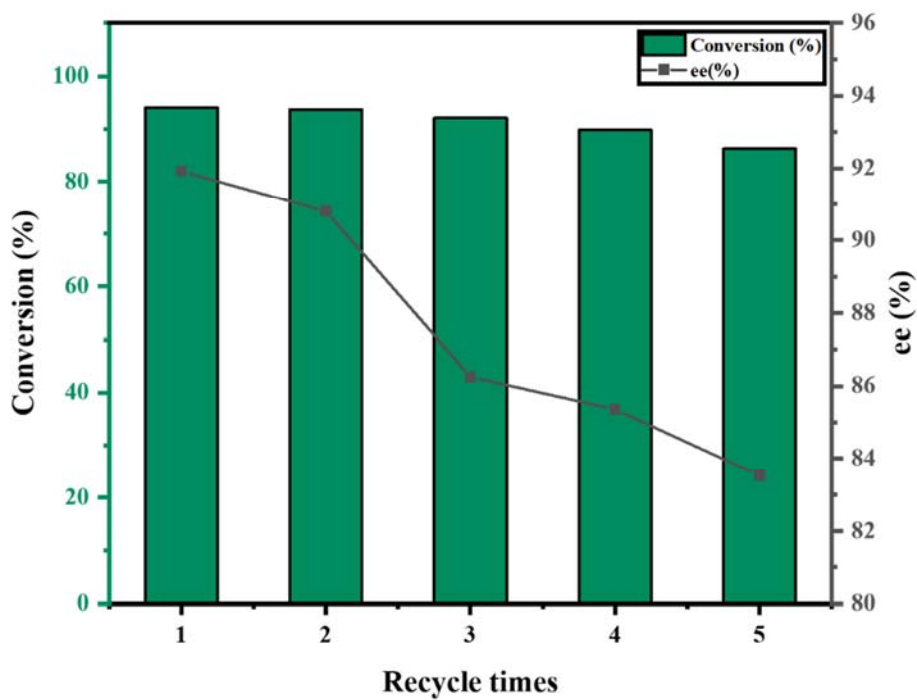


Figure 4.12 Recyclability test of encapsulated chiral Cu(II)-salen catalyst over chiral DHPM synthesis.

4.5.3 A comparative study for the synthesis of DHPMs

As shown in *Table 4.6*, a comparison has been provided for the synthesis of DHPMs using homogeneous and heterogeneous chiral catalytic systems. The results reveal that the present catalyst, i.e., encapsulated chiral Cu(II) salen complex has shown better catalytic activity in the shortest reaction time than the reported systems in terms of % conversion of DHPMs.^{10,84-90}

Table 4.6 A comparative study for the synthesis of DHPMs.

Entry	Catalysts	Conversion (%)	ee (%)	Reference
1	PAFMS-1	92	-	[10]
2	chiral phosphoric acid	85	95	[84]
3	(-)-4,5-Dimethyl-3,6-bis(o-tolyl)-1,2-benzenedisulfonimide	98	96	[85]
4	[Gmim]Cl-Cu(II)complex	96	98	[89]
5	Fe ₃ O ₄ @C@OSO ₃ H	93	-	[90]

4.6 Plausible catalytic pathway for the chiral DHPMs synthesis

There is still controversy surrounding Biginelli's reaction mechanism. Iminium, enamine, and Knoevenagel are the three most accepted mechanisms today. The progression of the mechanism and reaction pathways, nonetheless, has been deliberated in relation to reagents, ligands, and catalyst varieties. Drawing from the insights of Sweet and Fissekis, a conceptualization of the catalytic cycle governing the synthesis of DHPMs is typically postulated (*Figure 4.13*).⁹¹ Furthermore, certain catalytic conditions favour the Knoevenagel mechanism.⁹²

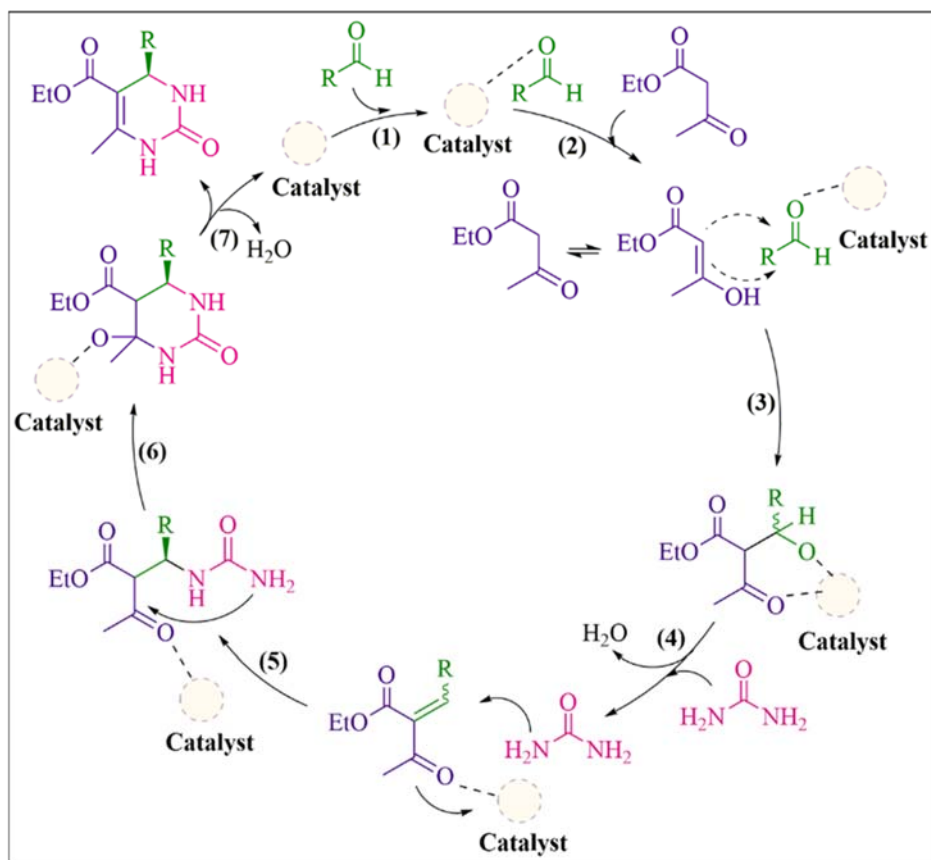


Figure 4.13 A plausible reaction pathway for the chiral DHPM synthesis using encapsulated chiral Cu(II) salen catalyst.

The catalytic cycle initiates with the introduction of the aldehyde (Step 1), which then proceeds to interact with the catalyst via a relatively weak catalyst-reactant bond (Step 2). Upon the addition of ethyl acetoacetate in Step 3, the enol form of the acetoacetate keto-enol equilibrium attacks the aldehyde bonded to the catalyst. This catalytic interaction leads to the formation of an adduct that expels water in Step 4. Upon introducing urea, Step 5 involves the creation of a C-N bond between urea and aldehyde (forming an iminium intermediate), thus imparting chirality that aligns with Kappe's proposed Lewis acid-catalyst mechanism in the Biginelli reaction. Subsequently, Step 6 involves the establishment of a new C-N bond between urea and ethyl acetoacetate. The ultimate step indicates catalyst regeneration, yielding the final product, DHPMs (Step 7), while simultaneously eliminating water to initiate a fresh cycle of catalyst.

4.7 Conclusions

To summarize, for the first time in the realm of heterogeneous chiral catalysis within the Biginelli reaction, present study have successfully devised an encapsulated chiral Cu(II)-salen complex. The chiral nature of the Schiff base ligand was revealed by a single crystal X-ray study of the salen ligand. Furthermore, the DFT study of an encapsulated chiral Cu(II)-salen complex confirms that the chirality is preserved during the encapsulation process. The encapsulated chiral Cu(II)-salen catalyst exhibited the highest catalytic efficacy in the asymmetric multicomponent Biginelli reaction. The product yields achieved varied from 91.7% to 96.1% across diverse substrates. The catalyst in question can be reused up to five times without significantly lowering the reaction yield. The asymmetric multicomponent Biginelli reaction's plausible catalytic mechanism was also proposed. The suggested approach, utilizing the innovative encapsulated chiral Cu(II)-salen catalyst, offers numerous advantages. These encompass a straightforward catalyst preparation procedure, brief reaction durations, environmentally benign conditions, and noteworthy product yields.

4.8 Crystallographic Data Information

Crystallographic information has been deposited with Cambridge Crystallographic Data Center, CCDC number **2181683**. The data can be obtained from through www.ccdc.cam.ac.uk/data_request/cif by e-mailing data request @ ccdc.cam.ac.uk, or by contacting The Cambridge Crystallography Data Center, 12 Union Road, Cambridge, CB2 IEZ, UK. Fax: þ44(0) 1223-336033.

4.9 References

1. Nicolaou, K. C. A new method for the one-step synthesis of α,β -unsaturated carbonyl systems from saturated alcohols and carbonyl compounds. *J. Am. Chem. Soc.* **2000**, 122, 7596-7597.
2. Shaabani, A., Soleimani, E., Maleki, A. & Rad, J. M. Rapid Synthesis of 3-Aminoimidazo [1,2-a] Pyridines and Pyrazines. *Synth. Commun.* **2008**, 38:7, 37–41.

3. Rotstein, B. H., Zaretsky, S., Rai, V. & Yudin, A. K. Small heterocycles in multicomponent reactions. *Chem. Rev.* **2014**, 114, 8323–8359.
4. Keihan, R. E., Radinekiyan, F., Aghamirza, H. & Aliabadi, M. Chitosan hydrogel/silk fibroin/Mg(OH)₂ nanobiocomposite as a novel scaffold with antimicrobial activity and improved mechanical properties. *Sci. Rep.* **2021**, 11:650, 1–13.
5. Taheri-ledari, R. Multi-Stimuli Nanocomposite Therapeutic : Docetaxel Targeted Delivery and Synergies in Treatment of Human Breast Cancer Tumor. *Small*, **2020**, 2002733, 1–20.
6. Andleeb, S., Imtiaz-ud-Din, I.-D., Rauf, M. K., Azam, S. S., Badshah, A., Sadaf, H., Raheel, A., Tahir, M. N., & Raza, S. A one-pot multicomponent facile synthesis of dihydropyrimidin-2(1: H)-thione derivatives using triphenylgermane as a catalyst and its binding pattern validation. *RSC Adv.* **2016**, 6, 79651–79661.
7. Wang, J. H. Novel bipyridinyl oxadiazole-based metal coordination complexes: High efficient and green synthesis of 3,4-dihydropyrimidin-2(1H)-ones through the Biginelli reactions. *J. Solid State Chem.* **2016**, 241, 86–98.
8. Huarig, Y., Yang, F. & Zhu, C. Highly enantioselective Biginelli reaction using a new chiral ytterbium catalyst: Asymmetric synthesis of dihydropyrimidines. *J. Am. Chem. Soc.* **2005**, 127, 16386–16387.
9. Chen, X. H., Xu, X. Y., Liu, H., Cun, L. F. & Gong, L. Z. Highly enantioselective organocatalytic Biginelli reaction. *J. Am. Chem. Soc.* **2006**, 128, 14802–14803.
10. Pramanik, M. & Bhaumik, A. Phosphonic Acid Functionalized Ordered Mesoporous Material: A New and Ecofriendly Catalyst for One-Pot Multicomponent Biginelli Reaction under Solvent-Free Conditions. *ACS Appl. Mater. Interfaces*, **2014**, 6, 933–941
11. Maleki, A., Hajizadeh, Z. & Firouzi-haji, R. Microporous and Mesoporous Materials Eco-friendly functionalization of magnetic halloysite nanotube with SO₃H for synthesis of dihydropyrimidinones. *Microporous Mesoporous Mater.* **2018**, 259, 46–53.
12. Grayson, D. H. & O'Donnell, S. H. Addition of nucleophiles to (E)-3-phenylsulfonylprop-2-enenitrile: A route to β -substituted α,β -unsaturated nitriles and to acetals of cyanoacetaldehyde. *Arkivoc* **2003**, 2003, 4–14.
13. Das, S. K., Chowdhury, A., Chakraborty, D., Kayal, U. & Bhaumik, A. Porous organic polymer bearing triazine and pyrene moieties as an efficient organocatalyst. *Mol. Catal.* **2020**, 497, 111198.

14. Peng, Y., Song, S., Liu, F., Yin, Z., Zhong, Y., Yi, X., Zheng, A., Schüth, F., & Gu, D. General Surface-Casting Synthesis of Mesoporous Metal Oxides with Hollow Structures and Ultrahigh Surface Areas. *Chem. Mater.* **2022**, 34, 7042–7057.
15. Pirhadi, L., Rangaswamy, A. & Soleimani, E. PO₃H₂-Functionalized Fe₃O₄@SiO₂ Core–Shell as an Efficient and Magnetic Nanocatalyst for the Preparation of Dihydropyrimidinones via Biginelli Condensation. *Polycycl. Aromat. Compd.* **2022**, 42, 4374–4385.
16. Maleki, A. & Rahimi, J. Synthesis of dihydroquinazolinone and octahydroquinazolinone and benzimidazoloquinazolinone derivatives catalyzed by an efficient magnetically recoverable GO-based nanocomposite. *J. Porous Mater.* **2018**, 25, 1789–1796.
17. Taheri-ledari, R., Rahimi, J. & Maleki, A. Synergistic catalytic effect between ultrasound waves and pyrimidine-2,4-diamine-functionalized magnetic nanoparticles: Applied for synthesis of 1,4-dihydropyridine pharmaceutical derivatives. *Ultrason. - Sonochemistry* **2019**, 59, 104737.
18. Karandikar, P. Cu/Co-salen immobilized MCM-41: Characterization and catalytic reactions. *Catal. Commun.* **2004**, 52, 69–74.
19. Kureshy, R. I., Das, A., Khan, N. U. H., Abdi, S. H. R. & Bajaj, H. C. Cu(II)-macrocylic [H₄]salen catalyzed asymmetric nitroaldol reaction and its application in the synthesis of α 1-adrenergic receptor agonist (R)-phenylephrine. *ACS Catal.* **2011**, 1, 1529–1535.
20. Belokon', Y. N., Davies, R. G. & North, M. A practical asymmetric synthesis of α -methyl α -amino acids using a chiral cu-salen complex as a phase transfer catalyst. *Tetrahedron Lett.* **2000**, 41, 7245–7248.
21. Cozzi, P. G. Metal-Salen Schiff base complexes in catalysis: Practical aspects. *Chem. Soc. Rev.* **2004**, 33, 410–421.
22. Chen, T., Wun, C. K. T., Day, S. J., Tang, C. C. & Lo, T. W. B. Enantiospecificity in achiral zeolites for asymmetric catalysis. *Phys. Chem. Chem. Phys.* **2020**, 22, 18757–18764.
23. Zhou, X.-F. & Tang, K. Zeolite-Encapsulated Co(II)[H₄]Salen and [H₂]Salen Complexes:Pulp Bleaching Catalysts with Enhanced Bleachability. *Cellul. Chem. Technol.* **2016**, 50, 1047–1053.
24. Yang, Y., Zhang, Y., Hao, S. & Kan, Q. Tethering of Cu(II), Co(II) and Fe(III) tetrahydro-salen and salen complexes onto amino-functionalized SBA-15: Effects of salen ligand

- hydrogenation on catalytic performances for aerobic epoxidation of styrene. *Chem. Eng. J.* **2011**, 171, 1356–1366.
25. Lakhani, P. & Modi, C. K. Asymmetric hydrogenation using covalently immobilized Ru-BINOL-AP@MSNs Catalayst. *New J. Chem.* **2023**.
 26. Beverina, L. & Salice, P. Squaraine compounds: Tailored design and synthesis towards a variety of material science applications. *European J. Org. Chem.* **2010**, 7, 1207–1225.
 27. Mondal, K. & Pan, S. C. Lewis Acid Catalyzed [3+3] Annulation of Donor–Acceptor Cyclopropanes with γ -Hydroxyenones: Access to Highly Functionalized Tetrahydropyrans. *European J. Org. Chem.* **2017**, 2017, 534–537.
 28. Gong, L. Z., Chen, X. H. & Xu, X. Y. Asymmetric organocatalytic biginelli reactions: A new approach to quickly access optically active 3,4-dihydropyrimidin-2-(1H)-ones. *Chem. - A Eur. J.* **2007**, 13, 8920–8926.
 29. Chu, W. Effect of Binder Type on MWW-Based Catalysts for the Liquid-Phase Alkylation Reaction of Benzene with Ethylene. *Ind. Eng. Chem. Res.* **2022**, 61, 2693–2700.
 30. Jin, S., Tao, G., Zhang, S., Luo, Y., Fu, W., Wang, Z., Gao, H., Sun, H., & Yang, W. A facile organosilane-based strategy for direct synthesis of thin MWW-type titanosilicate with high catalytic oxidation performance. *Catal. Sci. Technol.* **2018**, 8, 6076–6083.
 31. Zhou, Y. Enhanced Surface Activity of MWW Zeolite Nanosheets Prepared via a One-Step Synthesis. *J. Am. Chem. Soc.* **2020**, 142, 8211–8222.
 32. Choudhary A., Das B. and Ray S. Encapsulation of a Ni salen complex in zeolite Y: an experimental and DFT study. *Dalton Trans.* **2015**, 44, 3753.
 33. Sharma M., Das B., Karunakar G. V., Satyanarayana L., & Bania K. K. Chiral Ni-Schiff Base Complexes inside Zeolite-Y and Their Application in Asymmetric Henry Reaction: Effect of Initial Activation with Microwave Irradiation. *J. Phys. Chem. C* **2016**, 120, 13563–13573.
 34. Kumari S., Ramesh A., Das B. and Ray S. Zeolite-Y encapsulated cobalt(II) Schiff-base complexes employed for photocatalytic dye-degradation and upcycling CO₂. *Inorg. Chem. Front.* **2021**, 8, 1553
 35. Modi, C. K., Vithalani, R. S., Patel, D. S., Som, N. N. & Jha, P. K. Zeolite-Y entrapped metallo-pyrazolone complexes as heterogeneous catalysts: Synthesis, catalytic aptitude and computational investigation. *Microporous Mesoporous Mater.* **2018**, 261, 275–285.

36. Modi, C. K., Solanki, N., Vithalani, R. & Patel, D. Baeyer-Villiger oxidation of cyclopentanone over zeolite Y entrapped transition metal-Schiff base complexes. *Appl. Organomet. Chem.* **2018**, 32, 1–13.
37. Lakhani, P. & Modi, C. K. Spick-and-span protocol for designing of silica-supported enantioselective organocatalyst for the asymmetric aldol reaction. *Mol. Catal.* **2022**, 525, 112359.
38. Patel, D., Modi, C. K., Jha, P. K., Srivastava, H. & Kane, S. R. ZnO Nanoparticles Embedded on a Reduced Graphene Oxide Nanosheet (ZnO-NPs@r-GO) as a Proficient Heterogeneous Catalyst for a One-Pot A3-Coupling Reaction. *Eur. J. Inorg. Chem.* **2021**, 2021, 3578–3590.
39. Ahmad, A., Naqvi, S. R., Rafique, M., Nasir, H. & Sarosh, A. Synthesis, characterization and catalytic testing of MCM-22 derived catalysts for n-hexane cracking. *Sci. Rep.* **2020**, 10, 1–11.
40. Schwanke, A. & Pergher, S. Lamellar MWW-type zeolites: Toward elegant nanoporous materials. *Appl. Sci.* **2018**, 8, 1636.
41. Jakkidi Krishna Reddy, Kshudiram Mantri, Shruti Lad, Jagannath Das, Ganesan Raman, Raksh vir Jasra. Synthesis of Ce-MCM-22 and its enhanced catalytic performance for the removal of olefins from aromatic stream. *J. Porous Mater.* **2020**, 27, 1649–1658.
42. Shiryaev, A. A. A chiral (1R,2R)-N,N'-bis-(salicylidene)-1,2-diphenyl-1,2-ethanediamine Schiff base dye: synthesis, crystal structure, Hirshfeld surface analysis, computational study, photophysical properties and in silico antifungal activity. *J. Iran. Chem. Soc.* **2021**, 18, 2897–2911.
43. Baleizão, C. & Garcia, H. Chiral salen complexes: An overview to recoverable and reusable homogeneous and heterogenous catalysts. *Chem. Rev.* **2006**, 106, 3987–4043.
44. Yuan, G., Jiang, H., Zhang, L., Liu, Y. & Cui, Y. Metallosalen-based crystalline porous materials: Synthesis and property. *Coord. Chem. Rev.* **2019**, 378, 483–499.
45. Motokura, K., Ding, S., Usui, K. & Kong, Y. Enhanced Catalysis Based on the Surface Environment of the Silica-Supported Metal Complex. *ACS Catal.* **2021**, 11, 11985–12018.
46. Modi, C. K., Trivedi, P. M., Gupta, S. K. & Jha, P. K. Transition metal complexes enslaved in the supercages of zeolite-Y: DFT investigation and catalytic significance. *J. Incl. Phenom. Macrocycl. Chem.* **2012**, 74, 117–127.

47. Shaw, S. & White, J. D. Asymmetric Catalysis Using Chiral Salen-Metal Complexes: Recent Advances. *Chem. Rev.* **2019**, 119, 9381–9426.
48. Uhrmacher, F., Elbert, S. M., Rominger, F. & Mastalerz, M. Synthesis of Large [2+3] Salicylimine Cages with Embedded Metal-Salphen Units. *Eur. J. Inorg. Chem.* **2022**, 2022, 1–9.
49. Kargar, H. *et al.* Synthesis, spectral characterization, and theoretical investigation of Ni(II) and Pd(II) complexes incorporating symmetrical tetradentate Schiff base ligand: Suzuki-Miyaura cross-coupling reaction using PdLSym. *J. Iran. Chem. Soc.* **2022**, 19, 3981–3992.
50. Yimthachote, S., Chumsaeng, P. & Phomphrai, K. Complexity of imine and amine Schiff-base tin(ii) complexes: Drastic differences of amino and pyridyl side arms. *Dalt. Trans.* **2022**, 51, 509–517.
51. Yuan, Y. C., Mellah, M., Schulz, E. & David, O. R. P. Making Chiral Salen Complexes Work with Organocatalysts. *Chem. Rev.* **2022**, 122, 8841–8883.
52. Gbery, G., Zsigmond, A. & Balkus, K. J. Enantioselective epoxidations catalyzed by zeolite MCM-22 encapsulated Jacobsen's catalyst. *Catal. Letters* **2001**, 74, 77–80.
53. Sheldrick, G. M. SHELXT - Integrated space-group and crystal-structure determination. *Acta Crystallogr. Sect. A Found. Crystallogr.* **2015**, 71, 3–8.
54. Farrugia, L. J. WinGX suite for small-molecule single-crystal crystallography. *J. Appl. Crystallogr.* **1999**, 32, 837–838.
55. Farrugia, L. J. ORTEP-3 for windows - A version of ORTEP-III with a graphical user interface (GUI). *J. Appl. Crystallogr.* **1997**, 30, 565.
56. Spek, A. L. Structure validation in chemical crystallography. *Acta Crystallogr. Sect. D Biol. Crystallogr.* **2009**, 65, 148–155.
57. Valiey, E., Dekamin, M. G. & Alirezvani, Z. Sulfamic acid pyromellitic diamide-functionalized MCM-41 as a multifunctional hybrid catalyst for melting-assisted solvent-free synthesis of bioactive 3,4-dihydropyrimidin-2-(1H)-ones. *Sci. Rep.* **2021**, 11, 11199.
58. Do Nascimento, L. G. *et al.* Niobium Oxides as Heterogeneous Catalysts for Biginelli Multicomponent Reaction. *J. Org. Chem.* **2020**, 85, 11170–11180.
59. Mohammad Ali Nasser, Zinat Rezazadeh, Milad Kazemnejadi, Ali Allahresani. Cu-Mn Bimetallic Complex Immobilized on Magnetic NPs as an Efficient Catalyst for Domino One-Pot Preparation of Benzimidazole and Biginelli Reactions from Alcohols. *Catal. Lett.*

- 2021, 151, 1049–1067.
60. Patil, R. V., Chavan, J. U., Dalal, D. S., Shinde, V. S. & Beldar, A. G. Biginelli Reaction: Polymer Supported Catalytic Approaches. *ACS Comb. Sci.* **2019**, 21, 105–148.
 61. Fan-Jie Meng, Lei Shi, Guang-Shou Feng, Lei Sun, and Yong-Gui Zhou. Enantioselective Synthesis of 3,4-Dihydropyrimidin-2(1H)-ones through Organocatalytic Transfer Hydrogenation of 2-Hydroxypyrimidines. *J. Org. Chem.* **2019**, 84, 4435–4442.
 62. Heravi, M. M., Moradi, R., Mohammadkhani, L. & Moradi, B. Current progress in asymmetric Biginelli reaction: an update. *Mol. Divers.* **2018**, 22, 751–767.
 63. Alvim, H. G. O. Combined Role of the Asymmetric Counteranion-Directed Catalysis (ACDC) and Ionic Liquid Effect for the Enantioselective Biginelli Multicomponent Reaction. *J. Org. Chem.* **2018**, 83, 12143–12153.
 64. Thakkar, R. & Bandyopadhyay, R. Preparation, characterization, and post-synthetic modification of layered MCM-22 zeolite precursor. *J. Chem. Sci.* **2017**, 129, 1671–1676.
 65. Cao, S. “Desert Rose” MCM-22 microsphere: Synthesis, formation mechanism and alkylation performance. *Microporous Mesoporous Mater.* **2021**, 315, 110910.
 66. Juneau, M., Liu, R., Peng, Y., Malge, A., Ma, Z., & Porosoff, M. D. Characterization of Metal-zeolite Composite Catalysts: Determining the Environment of the Active Phase. *ChemCatChem* **2020**, 12, 1826–1852.
 67. Chen, J. Catalytic performances of cu/mcm-22 zeolites with different cu loadings in nh₃-scr. *Nanomaterials* **2020**, 10, 1–20.
 68. Srilai, S. Synthesis of zeolite A from bentonite via hydrothermal method: The case of different base solution. *AIP Conf. Proc.* **2020**, 2279, 060006.
 69. Magar R. R., Pawar G. T., Gadekar S. P., Lande M. K. Fe-MCM-22 catalyzed multicomponent synthesis of dihydropyrano [2,3-c] pyrazole derivatives. *Iran. J. Catal.* **2017**, 7(1), 1-9.
 70. Barakov, R. MWW-type zeolite nanostructures for a one-pot three-component Prins–Friedel–Crafts reaction. *Inorg. Chem. Front.* **2022**, 9, 1244.
 71. Modi, C. K. & Trivedi, P. M. Zeolite-Y based nanohybrid materials: Synthesis, characterization and catalytic aspects. *Microporous Mesoporous Mater.* **2012**, 155, 227–232.
 72. Carriço, C. S. MWW-type catalysts for gas phase glycerol dehydration to acrolein. *J. Catal.*

- 2016, 334, 34–41.
73. Kianfar, A. H. Experimental and theoretical structural determination, spectroscopy and electrochemistry of cobalt (III) Schiff base complexes: immobilization of complexes onto Montmorillonite-K10 nanoclay. *J. Iran. Chem. Soc.* **2018**, 15, 369–380.
 74. Sadhasivam, V., Sankar, B., Elamathi, G., Mariyappan, M. & Siva, A. Cu(OAc)₂ entrapped on ethylene glycol-modified melamine–formaldehyde polymer as an efficient heterogeneous catalyst for Suzuki–Miyaura coupling reactions. *Res. Chem. Intermed.* **2020**, 46, 681–700.
 75. Sharma, C., Kaur, M., Choudhary, A., Sharma, S. & Paul, S. Nitrogen Doped Carbon–Silica Based Cu(0) Nanometal Catalyst Enriched with Well-Defined N-moieties: Synthesis and Application in One-Pot Synthesis of 1,4-Disubstituted-1,2,3-triazoles. *Catal. Letters* **2020**, 150, 82–94.
 76. Abd El Khalk, A. A., Betiha, M. A., Mansour, A. S., Abd El Wahed, M. G. & Al-Sabagh, A. M. High Degradation of Methylene Blue Using a New Nanocomposite Based on Zeolitic Imidazolate Framework-8. *ACS Omega* **2021**, 6, 26210–26220.
 77. Chao, S. Nitrogen-doped Carbon Derived from ZIF-8 as a High-performance Metal-free Catalyst for Acetylene Hydrochlorination. *Sci. Rep.* **2017**, 7, 1–7.
 78. Vithalani, R. S., Patel, D., Modi, C. K., Jha, P. K., Srivastava, H., & Kane, S. R. Synthesis of less acidic VO-salen complex grafted onto graphene oxide via functionalization of surface carboxyl groups for the selective oxidation of norbornene. *Graphene Technol.* **2020**, 5, 83–101.
 79. Giannozzi, P. QUANTUM ESPRESSO: A modular and open-source software project for quantum simulations of materials. *J. Phys. Condens. Matter* **2009**, 21, 395502.
 80. Perdew, J. P. & Burke, K. Generalized gradient approximation for the exchange-correlation hole of a many-electron system. *Phys. Rev. B - Condens. Matter Mater. Phys.* **1996**, 54, 16533–16539.
 81. Momma, K. & Izumi, F. VESTA 3 for three-dimensional visualization of crystal, volumetric and morphology data. *J. Appl. Crystallogr.* **2011**, 44, 1272–1276.
 82. Wang, Y. A DFT study on isomorphously substituted MCM-22 zeolite. *J. Phys. Chem. A* **2004**, 108, 6730–6734.
 83. Chodvadiya, D., Jha, P. K. & Chakraborty, B. Theoretical inspection of Ni/ α -SiX (X=N, P,

- As, Sb, Bi) Single-Atom catalyst: Ultra-high performance for hydrogen evolution reaction. *Int. J. Hydrogen Energy* **2022**, *99*, 41733-41747.
84. Hu, X., Guo, J., Wang, C., Zhang, R. & Borovkov, V. Stereoselective Biginelli-like reaction catalyzed by a chiral phosphoric acid bearing two hydroxy groups. *Beilstein J. Org. Chem.* **2020**, *16*, 1875–1880.
85. Barbero, M., Cadamuro, S. & Dughera, S. A Brønsted acid catalysed enantioselective Biginelli reaction. *Green Chem.* **2017**, *19*, 1529–1535.
86. Gross, E. symmetric catalysis at the mesoscale: Gold nanoclusters embedded in chiral self-assembled monolayer as heterogeneous catalyst for asymmetric reactions. *J. Am. Chem. Soc.* **2013**, *135*, 3881–3886.
87. Al-Zaydi, K. M., Al-Boqami, M. & Elnagdi, N. M. H. Green Synthesis of Dihydropyrimidines and Pyridines Utilizing Biginelli Reaction. *Polycycl. Aromat. Compd.* **2021**, *0*, 1–12.
88. Ding, D. & Zhao, C. G. Primary amine catalyzed Biginelli reaction for the enantioselective synthesis of 3,4-dihydropyrimidin-2(1H)-ones. *European J. Org. Chem.* **2010**, *2*, 3802–3005.
89. Karthikeyan, P., Aswar, S. A., Muskawar, P. N., Bhagat, P. R. & Senthil Kumar, S. Development and efficient 1-glycyl-3-methyl imidazolium chloride-copper(II) complex catalyzed highly enantioselective synthesis of 3, 4-dihydropyrimidin- 2(1H)-ones. *J. Organomet. Chem.* **2013**, *723*, 154–162.
90. Taheri Hatkehlouei, S. F., Mirza, B. & Soleimani-Amiri, S. Solvent-Free One-Pot Synthesis of Diverse Dihydropyrimidinones/Tetrahydropyrimidinones Using Biginelli Reaction Catalyzed by Fe₃O₄@C@OSO₃H. *Polycycl. Aromat. Compd.* **2022**, *42*, 1341–1357.
91. Frederick. Sweet and John D. Fissekis, Synthesis of 3,4-dihydro-2(1H)-pyrimidinones and the mechanism of the Biginelli reaction. *J. Am. Chem. Soc.* **1973**, *95*, 26, 8741–8749.
92. Alvim, H. G. O., Da Silva Júnior, E. N. & Neto, B. A. D. What do we know about multicomponent reactions? Mechanisms and trends for the biginelli, hantzsch, mannich, passerini and ugi MCRs. *RSC Adv.* **2014**, *4*, 54282–54299.